J. Fluid Mech. (1996), *vol.* 316, *pp.* 307–324

On the linear instability of elliptic pipe flow

By R. R. KERSWELL† AND A. DAVEY

Department of Mathematics and Statistics, University of Newcastle upon Tyne, NE1 7RU, UK

(Received 14 June 1995 and in revised form 16 February 1996)

The linear stability of elliptic pipe flow is considered for finite aspect ratios thereby bridging the gap between the small-aspect-ratio analysis of Davey & Salwen (1994) and the large-aspect-ratio asymptotics of Hocking (1977). The flow is found to become linearly unstable above an aspect ratio of about 10.4 to the spanwise-modulated analogue of the Orr–Sommerfeld mode to which plane Poiseuille flow first loses stability. This disturbance is found to possess a series of intense vortices along its critical layer at lateral stations far removed from the central minor axis. The critical Reynolds number appears to fall from infinity as the aspect ratio increases above 10.4, ultimately approaching Hocking's (1977) asymptotic result at much larger aspect ratios.

1. Introduction

There is only a very small number of simple exact solutions to the Navier–Stokes equations and as a result the linear stability of these flows has been exhaustively studied – with one exception: the laminar flow in an elliptic pipe. Here, rather than the linear problem reducing to a one-dimensional eigenvalue problem, the asymmetry of the basic state means that a two-dimensional eigenvalue problem in the cross-space coordinates must be solved. A number of authors have made progress by considering an appropriately chosen limit of this full problem: large Reynolds number (Smith 1979), small ellipticity (Davey & Salwen 1994) and large aspect ratio (Hocking 1977). However, certainly at finite ellipticities and near the critical Reynolds number, extracting information from this eigenvalue problem appears viable only through numerical methods. These are used here to extend the initial work of Davey & Salwen (1994) to pipes of finite ellipticities and then ultimately to the large-aspect-ratio results of Hocking (1977).

Apart from the classical nature of the problem itself, elliptical pipe flow is of considerable interest by virtue of the gap it bridges between Hagen–Poiseuille flow (HPF) in a circular pipe and plane Poiseuille flow (PPF) in a channel. If the ellipticity of the pipe is small, so that the cross-section is almost a circle, then the flow approximates HPF which is generally believed to be stable to infinitesimal disturbances. Alternatively, when the ellipticity is large, so that the major axis of the ellipse is much longer that the minor axis, the flow approximates PPF and a critical Reynolds number almost certainly exists. The question then arises as to how and when (as a function of the ellipse's aspect ratio A) does a critical Reynolds number appear. Two *distinct possibilities* exist: the critical Reynolds number either tends to infinity or to a finite value as $A \to A_{crit}$ from above. For the latter case, the neutral

† Present address: Department of Mathematics, University of Bristol, BS8 1TW, UK.

curve in the wave number–Reynolds number plane must close and subsequently shrink to a point as A decreases to A_{crit}. For A slightly above A_{crit} in this scenario, linear instability would then only appear within a finite band of Reynolds numbers centred on the critical value. This band may remain finite for all finite A larger than A_{crit} or become semi-infinite at another critical aspect ratio A_∞. Underlying all this, however, is the issue of whether $A_{crit} > 1$, which would add yet further to the large body of evidence indicating that HPF is linearly stable for all Reynolds numbers.

At large aspect ratios, we are essentially studying how spanwise boundary curvature stabilizes PPF. Other studies to consider how PPF may be stabilized include adding a finite amount of streamwise shear motion to the boundary plates thereby setting up a mixture of PPF and plane Couette flow (PCF) (Potter 1966; Hains 1967; Reynolds & Potter 1967). Linear stability for all Reynolds numbers is then obtained if the speed of the plates exceeds 53% of the mean flow-through velocity (Reynolds & Potter 1967). Tatsumi & Yoshimura (1990) have studied the also stabilizing effect of imposing sidewalls on PPF by examining rectangular duct flow. Starting at the large-aspect-ratio PPF limit and working towards the square-duct limit, they estimated that the critical Reynolds number becomes infinite when the duct aspect ratio is about 3.2. The elliptic pipe flow problem tackled here is the exact complement to this work: we start at linearly stable HPF and then move smoothly away towards PPF by increasing the ellipticity in search of linear instability.

The analytical work of Hocking (1977,1978) hints at the relative importance of spanwise boundary curvature and the presence of sidewalls on the critical Reynolds number. For a rectangular duct of large aspect ratio, $A \gg 1$, he found using a regular perturbative approach that the PPF critical Reynolds number is only weakly increased by an amount $6844/A^2$. In contrast, for an elliptical pipe in which the boundary curvature is felt throughout, the effect is much stronger at $86\,300/A$. If anything, this would tend to suggest that elliptical pipe flow is stable beyond the aspect ratio of 3.2 at which rectangular duct flow first loses linear stability.

The plan of the paper is as follows. Section 2 formulates the eigenvalue problem to be solved in terms of a set of non-orthogonal elliptico-polar coordinates. These effectively restore the basic flow and crucially the boundary to that of circular pipe flow but at the minor expense of complicating the momentum equation to be solved. Section 3 discusses the numerical method used to solve the eigenvalue problem accompanied by an Appendix which details the symmetry arguments used to optimize the coding. The results are presented in §4 followed by a discussion in §5.

2. Formulation

We consider the linear stability of the basic Poiseuille flow

$$\boldsymbol{U} = \left(1 - \frac{x^2}{1+\beta} - \frac{y^2}{1-\beta}\right)\hat{\boldsymbol{z}} \tag{2.1}$$

through an elliptical pipe defined by

$$\frac{x^2}{1+\beta} + \frac{y^2}{1-\beta} = 1 \tag{2.2}$$

such that its aspect ratio is

$$A = \left(\frac{1+\beta}{1-\beta}\right)^{1/2}. \tag{2.3}$$

A natural transformation to make is to orthogonal elliptic cylindrical coordinates (ζ, η, z) where

$$x = \frac{\cosh\zeta}{\sinh\zeta_0}\cos\eta, \quad y = \frac{\sinh\zeta}{\sinh\zeta_0}\sin\eta, \tag{2.4}$$

with

$$0 \leqslant \eta < 2\pi, \quad 0 \leqslant \zeta \leqslant \zeta_0 = \tfrac{1}{2}\log\left(\frac{A+1}{A-1}\right).$$

However, this coordinate system is problematic for two reasons both of which essentially stem from the fact that, apart from at the boundary, it does not reflect the structure of the basic flow. Curves of constant ζ are confocal ellipses rather than the similar constant-speed ellipses of the basic flow and collapse as $\zeta \to 0$ to a singular line segment joining the foci on the major axis. This inevitably leads to a degradation in any numerical scheme based on this coordinate representation. Secondly and more seriously, any discretization matrices based on spectral expansions of the physical variables will be *dense* matrices due to the awkward form of the transformation. This severely limits the range of parameter space which can be explored computationally to the extent that linear instability of elliptical pipe flow cannot be reached.

A far more suitable system proves to be the non-orthogonal elliptico-polar coordinates (s, ϕ, z) defined by

$$x = s(1+\beta)^{1/2}\cos\phi, \quad y = s(1-\beta)^{1/2}\sin\phi \tag{2.5}$$

in which *both* the boundary ($s = 1$) and the basic flow field ($\boldsymbol{U} = (1-s^2)\hat{\boldsymbol{z}}$) depend on only the one coordinate s. The price paid for this simplification however is the increased complexity of the linearized momentum equation caused by the non-orthogonality of the transformation (2.5). Despite this, the equations are still separable in time and the axial variable z and these dependencies are removed from the velocity and pressure perturbations in the conventional way by introducing an axial wavenumber α and (complex) frequency $-\alpha c$ as follows:

$$[\boldsymbol{u}(s,\phi,z,t), P(s,\phi,z,t)] = [u(s,\phi)\tilde{\boldsymbol{s}} + v(s,\phi)\tilde{\boldsymbol{\phi}} + w(s,\phi)\hat{\boldsymbol{z}}, p(s,\phi)]\mathrm{e}^{\mathrm{i}\alpha(z-ct)} \tag{2.6}$$

where

$$\begin{aligned}\tilde{\boldsymbol{s}} &= \quad (1+\beta)^{1/2}\cos\phi\,\hat{\boldsymbol{x}} + (1-\beta)^{1/2}\sin\phi\,\hat{\boldsymbol{y}},\\ \tilde{\boldsymbol{\phi}} &= -(1+\beta)^{1/2}\sin\phi\,\hat{\boldsymbol{x}} + (1-\beta)^{1/2}\cos\phi\,\hat{\boldsymbol{y}}.\end{aligned}$$

Projecting out three independent components of the linearized momentum equation (see Kerswell 1994 for the details) gives *exactly*

$$\begin{aligned}\left[-\mathrm{i}\alpha c + \mathrm{i}\alpha(1-s^2)\right]u + \frac{1-\beta\cos2\phi}{1-\beta^2}\frac{\partial p}{\partial s} + \frac{\beta\sin2\phi}{1-\beta^2}\frac{1}{s}\frac{\partial p}{\partial\phi} &= \frac{1}{R}\left\{\left(\bar{\nabla}^2 - \frac{1+\beta\cos2\phi}{1-\beta^2}\frac{1}{s^2}\right)u\right.\\ &\left. + \left(-\frac{1+\beta\cos2\phi}{1-\beta^2}\frac{2}{s^2}\frac{\partial}{\partial\phi} - \frac{2\beta\sin2\phi}{1-\beta^2}\frac{1}{s}\frac{\partial}{\partial s} + \frac{2\beta\sin2\phi}{1-\beta^2}\frac{1}{s^2}\right)v\right\},\end{aligned} \tag{2.7}$$

$$\begin{aligned}\left[-\mathrm{i}\alpha c + \mathrm{i}\alpha(1-s^2)\right]v + \frac{\beta\sin2\phi}{1-\beta^2}\frac{\partial p}{\partial s} + \frac{1+\beta\cos2\phi}{1-\beta^2}\frac{1}{s}\frac{\partial p}{\partial\phi} &= \frac{1}{R}\left\{\left(\bar{\nabla}^2 - \frac{1+\beta\cos2\phi}{1-\beta^2}\frac{1}{s^2}\right)v\right.\\ &\left. + \left(\frac{1+\beta\cos2\phi}{1-\beta^2}\frac{2}{s^2}\frac{\partial}{\partial\phi} + \frac{2\beta\sin2\phi}{1-\beta^2}\frac{1}{s}\frac{\partial}{\partial s} - \frac{2\beta\sin2\phi}{1-\beta^2}\frac{1}{s^2}\right)u\right\}\end{aligned} \tag{2.8}$$

and

$$\left[-\mathrm{i}\alpha c + \mathrm{i}\alpha(1-s^2)\right] w - 2s\,u + \mathrm{i}\alpha\, p = \frac{1}{R}\bar{\nabla}^2 w, \tag{2.9}$$

where

$$\bar{\nabla}^2 = \frac{1-\beta\cos 2\phi}{1-\beta^2}\frac{\partial^2}{\partial s^2} + \frac{1+\beta\cos 2\phi}{1-\beta^2}\frac{1}{s}\frac{\partial}{\partial s} + \frac{1+\beta\cos 2\phi}{1-\beta^2}\frac{1}{s^2}\frac{\partial^2}{\partial \phi^2} + \frac{2\beta\sin 2\phi}{1-\beta^2}\frac{1}{s}\frac{\partial^2}{\partial s\partial\phi} - \frac{2\beta\sin 2\phi}{1-\beta^2}\frac{1}{s^2}\frac{\partial}{\partial\phi} - \alpha^2$$

and R is a Reynolds number based upon the central flow speed of the basic state and a length scale in which the semi-major axis of the pipe measures $(1+\beta)^{1/2}$. As the cross-sectional area of the pipe is $(1-\beta^2)^{1/2}$ in these units, a more sensible choice for an elliptical pipe Reynolds number is

$$Re_{pipe} = (1-\beta^2)^{1/4} R \tag{2.10}$$

which when constant ensures that the flow rate down the pipe is independent of the ellipticity β. Working to $O(\beta)$, Davey & Salwen (1994) used R as their Reynolds number which at this order is then identical to Re_{pipe}. For comparison with PPF, alternative definitions of the Reynolds number and the axial wavenumber based on the semi-minor axis as the length scale are as follows:

$$Re_{ppf} = (1-\beta)^{1/2} R = \left(\frac{1-\beta}{1+\beta}\right)^{1/4} Re_{pipe}, \quad \alpha_{ppf} = \frac{\alpha}{(1-\beta)^{1/2}}. \tag{2.11}$$

The form of the incompressibility condition is preserved under the transformation (2.5):

$$\frac{1}{s}\frac{\partial(su)}{\partial s} + \frac{1}{s}\frac{\partial v}{\partial\phi} + \mathrm{i}\alpha w = 0. \tag{2.12}$$

The equations (2.7)–(2.9) and (2.12) together with the non-slip boundary conditions

$$u = v = w = 0 \quad \text{at } s = 1 \tag{2.13}$$

constitute an eigenvalue problem for the complex frequency $-\alpha c$. The eigenvalue corresponding to the least-damped or most unstable disturbance *at a given axial wavenumber* α has the largest value of $\mathrm{Im}(\alpha c)$. Crucially, the coefficients in this eigensystem depend only on ϕ through either the functions $\cos 2\phi$ or $\sin 2\phi$. As a result, spectrally expanding the flow variables using Fourier modes in ϕ is very efficient as it ultimately leads to block-tridiagonal discretization matrices. It is essentially this feature alone which allows high enough Reynolds numbers and aspect ratios to be reached for linear instability to be seen.

3. Numerics

3.1. *Method*

Three different numerical formulations were examined. Firstly, the axial velocity w and the pressure p were eliminated using (2.12) and (2.9) respectively leaving two equations in the two variables u and v. Secondly, the poloidal-toroidal decomposition $\boldsymbol{u} = \nabla\times(\psi\tilde{\boldsymbol{s}}) + \nabla\times\nabla\times(\chi\tilde{\boldsymbol{s}})$ was used, again reducing the problem down to two equations in the two unknowns ψ and χ. Lastly, the eigenvalue problem was solved as it stood, that is all four variables u, v, w and p were expanded directly. In each,

(u,v,w,p) with symmetries		(u,v,w,p)		(u,v) with symmetries	
N	αc_i $(\times 10^{-2})$	N	αc_i $(\times 10^{-2})$	N	αc_i $(\times 10^{-2})$
10	−3.868976161	20	−5.655564974	20	−4.141703421
15	−4.126329179	24	−4.190690188	25	−4.127535011
18	−4.128171613	28	−4.130039154	30	−4.127564486
20	−4.127555452	32	−4.127636991	35	−4.127564474
24	−4.127564418	36	−4.127565985	40	−4.127563718
28	−4.127564469	38	−4.127564277	50	−4.127564260
30	−4.127564469	40	−4.127564491	60	−4.127671038
40	−4.127564469	45	−4.127564469	70	−4.127503785
50	−4.127564469	50	−4.127564469	80	−4.127563842
80	−4.127564469	80	−4.127564469	90	−4.127569740
100	−4.127564469	100	−4.127564469	100	−4.127611556

TABLE 1. Convergence of the least-damped eigenvalue for the circular pipe case ($\beta = 0$) given by the (u,v,w,p) code with and without radial symmetries built-in and the (u,v) code at $Re_{pipe} = 3000$ and $\alpha = 1$. The radial truncation parameter is N for all expansions and $M = 1$. Hence for the (u,v) code, the matrices are $2N \times 2N$, whereas for the (u,v,w,p) code, the matrices are $4N \times 4N$. The associated real part of the frequency is $c_r = 0.91146567$ and all computations were performed in double-precision arithmetic.

the relevant flow variables were approximated using double sums of Fourier modes in ϕ and Chebyshev polynomials in s, before the governing equations were imposed through collocation over s and Galerkin projection in ϕ.

Although the last approach appears the least memory efficient of the three, it proved by far the most practical owing to the simplicity of coding, the absence of spurious eigenvalues and its stable convergence properties. Even though the first two cases would converge earlier (in terms of storage requirements) to the correct eigenvalue, this value would then wander disconcertingly under increased truncation and rogue eigenvalues would always be present – see table 1 which details this behaviour for the (u,v) code at $Re_{pipe} = 3000$, $\alpha = 1$ and $\beta = 0$. Presumably, the two high-order equations solved in the bivariable cases are slightly ill-conditioned by the coordinate singularity at the axis of the pipe.† Although in itself small, this effect prevented precise comparison with known analytic results at small ellipticity β (Davey & Salwen 1994) and hence crucial checks on the code were unavailable. In contrast, the third approach invariably yielded a 'clean' set of eigenvalues (half of which would be infinite corresponding to compressible disturbances) and delivered robust convergence as evidenced in table 1. Excellent agreement was achieved with the small-ellipticity results of Davey & Salwen (1994) for $\beta \leqslant 0.1$. The only disadvantage of the third approach is its larger storage requirement compared with the other cases. However, this is not as severe as it first appears because the representation of each physical variable through its own expansion is more efficient than indirectly expanding a subset. By way of illustration, table 1 shows that $N = 20$ (80 coefficients) for the (u,v,w,p) with-symmetries (see below) code is sufficient to achieve 5 significant figures in the decay rate as opposed to $N = 30$ (60 coefficients) for the (u,v) with-symmetries code.

† This behaviour persisted despite reformulating the equations in terms of $f = su$ and $g = sv$ and explicitly imposing regularity conditions at the axis.

The eigenfunctions possess definite parities in both ϕ and s owing to (i) the reflectional symmetry of the system in the major and minor axes and (ii) the representation degeneracy afforded by cylindrical coordinates. The former feature means that the eigenfunctions can be partitioned into solutions with just even or just odd Fourier modes and then these modes further subdivided into those symmetric or antisymmetric about the minor axis. The latter feature implies that the radial structure of these 'even' or 'odd' eigenfunctions also possess definite symmetries or parities in s – the Appendix discusses this important idea for both cylindrical and spherical polar coordinates systems. The upshot of all this is that we may search separately for four different types of mode:

$$\begin{bmatrix} u \\ v \\ w \\ p \end{bmatrix} = \sum_{m=1}^{M}\sum_{n=1}^{N} \left.\begin{bmatrix} u_{nm}\Theta_{2n}(s)\sin(2m-1)\phi \\ v_{nm}\Theta_{2n}(s)\cos(2m-1)\phi \\ w_{nm}\Theta_{2n+1}(s)\sin(2m-1)\phi \\ p_{nm}T_{2n-1}(s)\sin(2m-1)\phi \end{bmatrix}\right\} \text{type I}: w(\mathrm{a},\mathrm{s}), \begin{pmatrix} + & + \\ - & - \end{pmatrix}, \quad (3.1)$$

$$\begin{bmatrix} u \\ v \\ w \\ p \end{bmatrix} = \sum_{m=1}^{M}\sum_{n=1}^{N} \left.\begin{bmatrix} u_{nm}\Theta_{2n+1}(s)\sin 2(m-1)\phi \\ v_{nm}\Theta_{2n+1}(s)\cos 2(m-1)\phi \\ w_{nm}\Theta_{2n}(s)\sin 2(m-1)\phi \\ p_{nm}T_{2n-2}(s)\sin 2(m-1)\phi \end{bmatrix}\right\} \text{type II}: w(\mathrm{a},\mathrm{a}), \begin{pmatrix} - & + \\ + & - \end{pmatrix}, \quad (3.2)$$

$$\begin{bmatrix} u \\ v \\ w \\ p \end{bmatrix} = \sum_{m=1}^{M}\sum_{n=1}^{N} \left.\begin{bmatrix} u_{nm}\Theta_{2n+1}(s)\cos 2(m-1)\phi \\ v_{nm}\Theta_{2n+1}(s)\sin 2(m-1)\phi \\ w_{nm}\Theta_{2n}(s)\cos 2(m-1)\phi \\ p_{nm}T_{2n-2}(s)\cos 2(m-1)\phi \end{bmatrix}\right\} \text{type III}: w(\mathrm{s},\mathrm{s}), \begin{pmatrix} + & + \\ + & + \end{pmatrix}, \quad (3.3)$$

$$\begin{bmatrix} u \\ v \\ w \\ p \end{bmatrix} = \sum_{m=1}^{M}\sum_{n=1}^{N} \left.\begin{bmatrix} u_{nm}\Theta_{2n}(s)\cos(2m-1)\phi \\ v_{nm}\Theta_{2n}(s)\sin(2m-1)\phi \\ w_{nm}\Theta_{2n+1}(s)\cos(2m-1)\phi \\ p_{nm}T_{2n-1}(s)\cos(2m-1)\phi \end{bmatrix}\right\} \text{type IV}: w(\mathrm{s},\mathrm{a}), \begin{pmatrix} - & + \\ - & + \end{pmatrix}. \quad (3.4)$$

Here we have adopted the modal I–IV nomenclature of Tatsumi & Yoshimura (1990), where, for instance, w(a,s) means that the axial velocity w is antisymmetric and symmetric with respect to the major and minor axes respectively. Here $T_n(s) = \cos(n\cos^{-1}s)$ is the nth Chebyshev polynomial and

$$\Theta_n(s) \equiv T_n(s) - T_{n-2}(s) \quad (3.5)$$

so that the boundary conditions are built into the spectral functions.

Computationally, rather than viewing the interior of the pipe as the region $\{0 \leqslant s \leqslant 1, -\pi \leqslant \phi < \pi\}$, we consider the equivalent domain $\{-1 \leqslant s \leqslant 1, 0 \leqslant \phi < \pi\}$. The solution in $-1 \leqslant s < 0$ can be constructed from that in $0 < s \leqslant 1$ through the known symmetries and so we need only collocate the equations over the positive zeros of $T_{2N}(s)$ and impose boundary conditions at $s = 1$. This approach is in contrast to the normal technique of expanding in modified Chebyshev polynomials $T_n(2s-1)$, $n = 0, 1, 2, \ldots, N$, collocating over, say, the Gauss–Lobatto points $s_j = \frac{1}{2}(\cos[j\pi/(N-1)] + 1)$, $j = 1, 2, \ldots, N-1$ (Schmid & Henningson 1994; O'Sullivan & Breuer 1994) and explicitly imposing the regularity conditions

$$(m \pm 1)(\mathrm{i}u \mp v) = \mathrm{i}mw = \mathrm{i}mp = 0 \quad (3.6)$$

at the axis (Batchelor & Gill 1962; Davey 1978). By building the appropriate radial parities into the expansions, the correct axial behaviour automatically follows without need to explicitly impose the regularity conditions (3.6), and storage requirements can be quartered (see table 1). Most important, however, is that the collocation

	(u, v, w, p) with symmetries		(u, v, w, p)	
αRe	N	αc_i $(\times 10^{-3})$	N	αc_i $(\times 10^{-3})$
10^4	25	−22.70608805	30	−21.97711837
	30	−22.70490056	40	−22.70501396
	35	−22.70491459	45	−22.70493910
	40	−22.70491455	50	−22.70491463
	50	−22.70491455	60	−22.70491455
10^5	30	−6.928706156	45	−6.968942673*
	35	−7.195471472	50	−7.310500588*
	40	−7.210044934	55	−7.223205443
	45	−7.202142015	60	−7.204790614
	50	−7.202214757	70	−7.202331463
	55	−7.202317618	80	−7.202308193
	60	−7.202307690	90	−7.202308050
	70	−7.202308049	100	−7.202308058
	80	−7.202308049	120	−7.202308029
10^6	50	−2.036937516	60	−1.659436401*
	60	−2.274192895	70	−2.135542968*
	70	−2.282792323	80	−2.289035815*
	80	−2.279561805	90	−2.279634661*
	90	−2.279629961	100	−2.279630812*
	100	−2.279649954	110	−2.279648057*
	110	−2.279647891	120	−2.279648122
	120	−2.279647999	140	−2.279647993

TABLE 2. Convergence of the least-damped (centre) eigenvalue for the circular pipe case ($\beta = 0$ and therefore $M = 1$) using the (u, v, w, p) codes with and without the radial symmetries built-in at $\alpha = 1$ and $Re_{pipe} = 10^4$ ($c_r = 0.95148$), 10^5 ($c_r = 0.98465$) and 10^6 ($c_r = 0.995145$). The * indicates that spurious realistic eigenvalues were also generated. All computations were performed in double-precision arithmetic.

points are at their sparsest near the axis, $O(1/2N)$ spacing, rather than at their densest, $O(1/N^2)$ spacing. Desensitizing the code to the coordinate axis in this way is absolutely crucial when the need arises to approximate increasingly two-dimensional flow fields in ellipses of large aspect ratio within the confines of a polar coordinate system. Moving the collocation points from the centre to the wall is clearly advantageous for representing the 'wall' modes, to one of which PPF is unstable, but not the centre modes which are the most important pipe disturbance at large αRe_{pipe}. However, their localization is comparatively weak, being concentrated within a radius $O((\alpha Re_{pipe})^{-1/4})$ of the axis (Davey & Nguyen 1971), and the code with radial parities built-in still proves more efficient even up to $\alpha Re_{pipe} = 10^6$ – see table 2.

As mentioned previously, the governing equations only couple the Fourier mode m with nearest neighbours $m \pm 2$ ensuring that the discretization matrices are banded. This was exploited by both an inverse-iterative and a time-stepping approach (both requiring storage $O(MN^2)$) to achieve much higher truncations than possible with a full eigenvalue code where the storage is a prohibitive $O(M^2N^2)$.

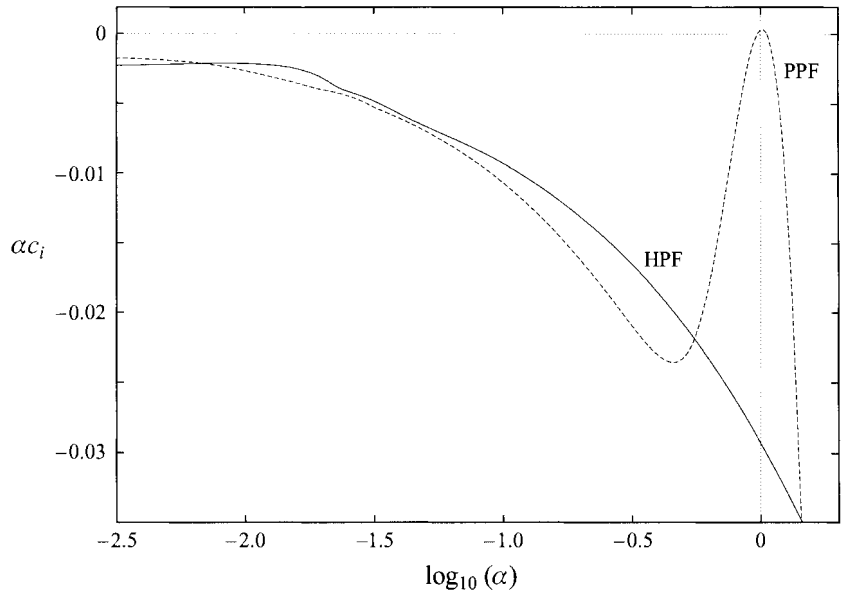

FIGURE 1. A plot of the minimum damping rate αc_i verses $\log_{10}(\alpha)$, where α is the axial wavenumber, for Hagen–Poiseuille flow (HPF) and plane Poiseuille flow (PPF) at $Re_{pipe} = Re_{ppf} = 6000$.

4. Results

It is now well established that plane Poiseuille flow first loses linear stability at a Reynolds number of 5772.22 to a two-dimensional wall mode (Orszag 1971). For a large enough aspect ratio, we can be confident that elliptic pipe flow will similarly be unstable to the three-dimensionally modulated analogue of this wall mode at some modified (larger) Reynolds number. What is not so clear is whether other modes, special to the elliptical geometry, become unstable first, i.e. that elliptic pipe flow might harbour some interesting intermediary behaviour of its own (in other words, does the decay rate–axial wavenumber curve for elliptic pipe flow break through the axis unexpectedly at it evolves from the HPF limit to the PPF limit – see figure 1). This seems unlikely but is not impossible. In fact, just such unexpected behaviour has been found by Cowley & Smith (1985) in plane Poiseuille–Couette flow, where two and sometimes three neutral curves can exist.

The natural place to look for such behaviour is at long axial wavelengths ($\alpha = O(Re_{pipe}^{-1})$) which are the least-damped eigenmodes in HPF (see figure 1 and Gill 1973) and accordingly appear the most easily destabilized (e.g. Mackrodt 1976). Smith (1979) also suggests that such long-wavelength modes will be important in elliptic pipe flow until a match with PPF is achieved at aspect ratios of $O(Re_{ppf}^{1/7})$. In addition, the perturbation analysis of Davey & Salwen (1994) for nearly circular elliptic pipes emphasizes the role of these long-wavelength disturbances, tentatively predicting that one should become unstable at only $A \approx 1.3$.

Numerically, the asymptotic parameter range $\alpha_{ppf} = O(Re_{ppf}^{-1})$ is reasonably accessible and the general trend with aspect ratio clear by $A = 6$. Figure 2 shows how the decay rate of the least-damped mode, which is of type IV (see (3.4)) in this regime, varies with $\log_{10}(\alpha_{ppf})$ at $Re_{ppf} = 6000$. The overall maximum modal growth rate in HPF ($A = 1$) at this Reynolds number is located at about $\alpha = \alpha_{ppf} = 10^{-2}$. Rather than this maximum being maintained and gradually rising to pierce the axis, increas-

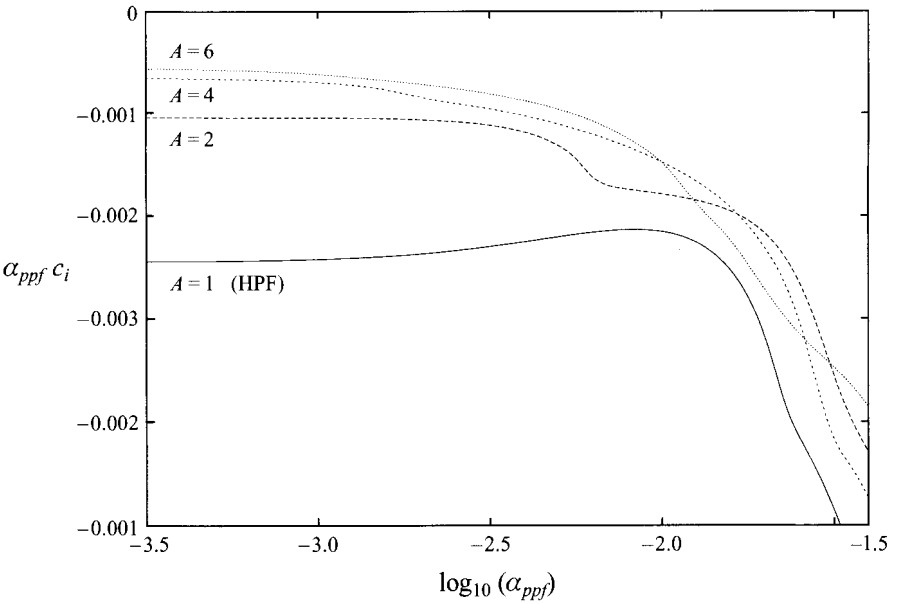

FIGURE 2. The minimum decay rate $\alpha_{ppf} c_i$ plotted at long wavelengths for varying aspect ratios A and $Re_{ppf} = 6000$. The well-known maximum at $\alpha = \alpha_{ppf} \approx 10^{-2}$ for HPF is quickly lost as A is increased ensuring that instability cannot occur in this regime. As $\alpha_{ppf} \to 0$, all the damping rates tend to a value which scales with Re_{ppf}^{-1}.

ing the aspect ratio quickly converts the decay rate curve into a steadily decreasing profile and the local peak is lost. The least-stable mode is then attained as $\alpha \to 0$ in this long-wavelength regime. The corresponding minimum decay rate always remains positive with increasing Reynolds number – in fact scaling with Re_{ppf}^{-1} – so that the whole curve remains below the axis. As a result, it seems clear that although the long-wavelength modes may be the least-damped modes for elliptic pipes of low aspect ratio, they do not actually become unstable.

Further computations of the least-damped eigenvalue over the four types of mode I–IV in the parameter ranges $10^{-4} \leqslant \alpha \leqslant 10^2$, $\alpha Re_{pipe} \leqslant 10^6$ and $A \leqslant 5$, reveal decay rate–$\log_{10}(\alpha_{ppf})$ curves which remain qualitatively similar to that of HPF rather than PPF (see figure 1). Beyond this parameter range, we could no longer afford the luxury of calculating all the eigenvalues for a particular modal type at given α, Re_{pipe} and A, and then using inverse iteration to 'polish up' the least-damped value. More extreme parameter ranges were reached by time-stepping the equations to just isolate the least-damped mode before again using inverse iteration to improve accuracy. Unfortunately, run times at large Reynolds numbers (e.g. $Re_{pipe} > 10^4$) soon became prohibitive due to the increasing stiffness of the system: a small incremental time step is forced by the fast modal frequencies but a long overall integration time required to differentiate between two slowly decaying neighbouring modes. However, by this stage, it had already become reasonably clear that no new instability would arise other than the PPF-type at sufficiently large aspect ratio. The search for linear instability was then accordingly tailored to this scenario.

Plane Poiseuille flow is linearly unstable to only one two-dimensional Orr–Sommerfeld mode for which the streamwise (axial) velocity component is antisymmetric about the midplane (major axis) (Orszag 1971). Along with this mode, there are, of course, other three-dimensional modes with similar symmetry which can be-

A	Re_{ppf}	α_{ppf}	c_r	A	Re_{ppf}	α_{ppf}	c_r
10.79	80000	0.712	0.140	17	18300	0.88	0.201
10.98	70000	0.726	0.144	18.5	16100	0.895	0.207
11.11	65000	0.733	0.147	20	14600	0.91	0.213
11.26	60000	0.742	0.150	21	13800	0.915	0.215
11.45	55000	0.752	0.153	23	12600	0.925	0.220
11.67	50000	0.763	0.157	25	11670	0.935	0.224
12	44000	0.775	0.162	30	10190	0.95	0.231
12.5	37900	0.795	0.168	35	9300	0.96	0.236
13	33200	0.81	0.174	40	8700	0.97	0.240
14	26900	0.83	0.183	45	8280	0.975	0.243
15	23000	0.85	0.190	50	7960	0.98	0.245
16	20300	0.865	0.196	∞	5772	1.02	0.264

TABLE 3. Numerical data for the neutral curve of elliptic pipe flow. The aspect ratio is A, Re_{ppf} is the critical Reynolds number and α_{ppf} the critical axial wavenumber both based on the semi-minor length scale. c_r is the modal frequency.

come linearly unstable but always at higher Reynolds numbers (Squire's theorem). Assuming that a similar situation pertains in a large-aspect-ratio elliptic pipe (i.e. an analogue of Squire's theorem holds at large but finite aspect ratio), we can confine attention to modes of type I. The spanwise-modulated two-dimensional PPF mode envisaged by Hocking (1977) is of this type. Modes of form II will be unstable later owing to their inherent three-dimensionality and modes symmetric about the midplane, III and IV, should always be stable. This picture is confirmed by Tatsumi & Yoshimura (1990) for Poiseuille flow through a rectangular duct where the basic flow differs more substantially from PPF than elliptic pipe flow with changing aspect ratio.

The least-damped mode of type I at $Re_{ppf} = 6000$ and $A = 10$ was found by time-stepping to be the spanwise-modulated analogue of the unstable two-dimensional PPF mode. This was clear through the close coincidence of their frequencies: only the decay rate changes appreciably as A decreases from infinity. Inverse iteration was then used to track this mode to more extreme values of the Reynolds number and aspect ratio until instability was found: see table 3. Fortunately, the spanwise-modulated PPF mode which determines the linear stability boundary is comparatively easy to resolve numerically. However, even in this case, the required truncation levels (N, M) did vary considerably along the neutral curve to the point where they had to be continually monitored. Tables 4 and 5 show typical truncation results for two extreme cases of large Reynolds number and large aspect ratio just above the neutral curve. Figure 3 shows the neutral stability curve in the (Re_{ppf}, A)-plane and figure 4 the critical axial wavenumber α_{ppf} and frequency c_r as a function of the aspect ratio. The critical Reynolds number Re_{ppf} appears to 'fall' from infinity at just over $A = 10$ and then gradually and monotonically approaches Hocking's asymptotic result

$$Re_{ppf} = 5772 + \frac{86\,300}{A}$$

as A increases. (In fact, the data tend to indicate a slightly different asymptotic

c_r / $c_i(\times 10^{-4})$	N=80	90	95	100	105	110
M=18	0.150064	0.150065	0.150065	0.150065	0.150065	0.150065
	1.15695	1.18683	1.18240	1.18339	1.18347	1.18338
20	0.150064	0.150065	0.150065	0.150065	0.150065	0.150065
	1.14396	1.17023	1.16589	1.16673	1.16687	1.16676
22	0.150063	0.150065	0.150065	0.150065	0.150065	0.150065
	1.14705	1.17385	1.16924	1.17010	1.17028	1.17015
25	0.150063	0.150065	0.150065	0.150065	0.150065	0.150065
	1.14681	1.17352	1.16879	1.16969	1.16988	1.16974
28	0.150063	0.150065	0.150065	0.150065	0.150065	
	1.14657	1.17337	1.16858	1.16950	1.16970	
30	0.150063	0.150065	0.150065	0.150065		
	1.14657	1.17337	1.16857	1.16950		

TABLE 4. Estimates of the most unstable eigenvalue (c_r upper entry and $c_i(\times 10^{-4})$ lower entry) using various truncation levels (N, M) for slightly supercritical elliptic pipe flow of aspect ratio $A = 11.4$, $\alpha_{ppf} = 0.742$ and $Re_{ppf} = 60000$.

c_r / $c_i(\times 10^{-4})$	N=40	45	50	55	60
M=45	0.244041	0.244040	0.244042	0.244042	0.244039
	1.33950	1.32385	1.32354	1.131696	1.33544
50	0.244039	0.244040	0.244040	0.244040	0.244040
	1.36191	1.32988	1.33002	1.33004	1.33025
55	0.244039	0.244040	0.244040	0.244040	0.244040
	1.31586	1.32944	1.32984	1.32986	1.32986
60	0.244040	0.244040	0.244040	0.244040	
	1.37508	1.33031	1.32986	1.32986	
70	0.244038	0.244040	0.244040		
	1.36214	1.32919	1.32986		
80	0.244038	0.244040			
	1.32869	1.32932			

TABLE 5. As table 4 but for $A = 50$, $\alpha_{ppf} = 0.9775$ and $Re_{ppf} = 8100$.

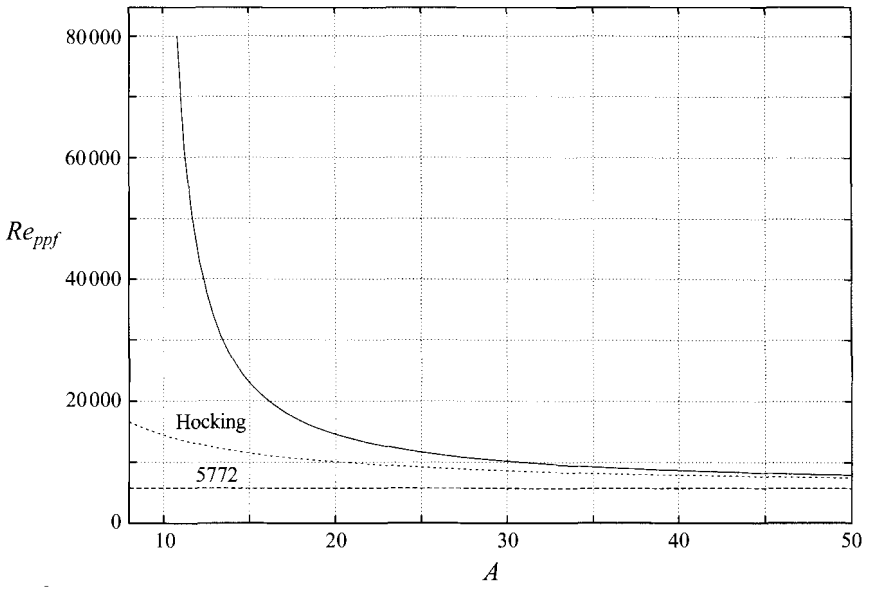

FIGURE 3. The neutral stability curve (solid line) for elliptic pipe flow in the (Re_{ppf}, A)-plane. Hocking's asymptotic result $Re_{ppf} = 5772 + 86\,300/A$ (short dash) and the PPF limiting value of 5772 (long dash) are also shown for comparison.

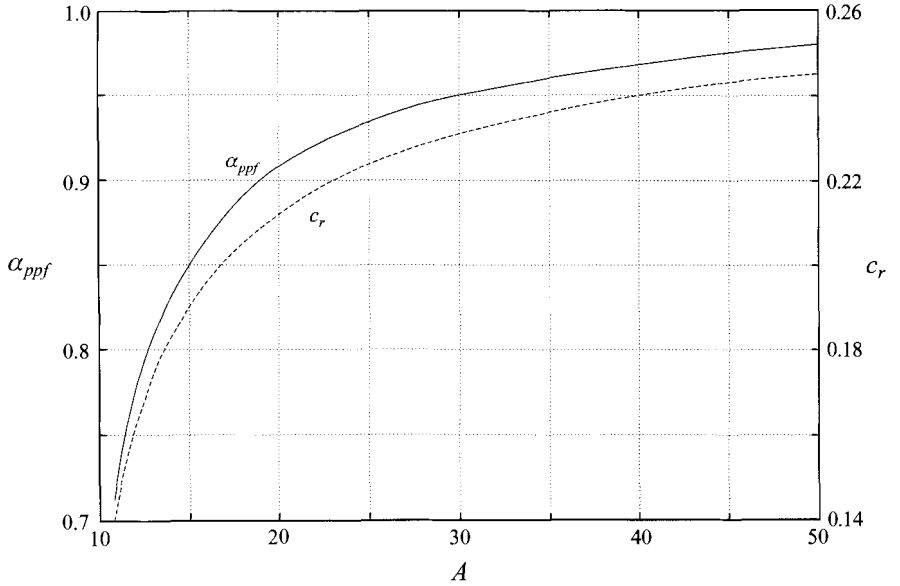

FIGURE 4. The variation of the critical axial wavenumber α_{ppf} and frequency c_r with the aspect ratio along the neutral curve. Limiting values should be $\alpha_{ppf} = 1.02$ and $c_r = 0.264$ as $A \to \infty$.

expression of the form

$$Re_{ppf} = 5772 + \frac{86\,300}{A - A_0} \tag{4.1}$$

with $A_0 \approx 10.6$, which is essentially just the next higher-order form of Hocking's result.) That the approach should be slow is apparent from the spanwise modulation

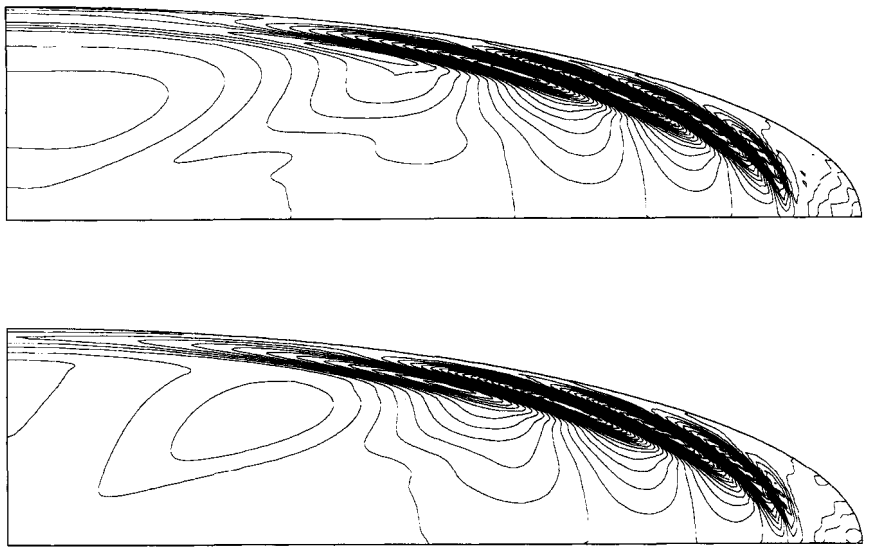

FIGURE 5. Contour plots of the axial velocity component (upper plot is Re(w) and lower Im(w)) just above criticality ($Re_{ppf} = 60\,000$, $\alpha_{ppf} = 0.742$, $c_r = 0.150065$) for a pipe of aspect ratio $A = 11.4$. The plot has been scaled down laterally by a factor of 11.4/4 and only the first quadrant is shown (there is symmetry with respect to the minor vertical axis and antisymmetry about the major horizontal axis). The truncation used is $N = 90$ and $M = 25$. The phase of the eigenfunctions has been chosen so that Im($w(x = 0, y = 0.5)$) = 0 and then normalized (max Re(w) = 1, max Im(w) = 0.999). The contour interval in both plots is 0.05. Note the presence of intense vortices along the critical layer far removed from the central region.

envisaged by Hocking in which the amplitude essentially varies laterally as

$$e^{-(0.05-0.90i)x^2/A}.$$

The dominant feature is then a spanwise oscillation of wavelength $2.6A^{1/2}$ riding upon a slow exponential decay of characteristic scale $(20A)^{1/2}$. Formally, Hocking's asymptotic analysis would seem to require $\sqrt{20} \ll A^{1/2}$ and as a result $A = 50$ is clearly still not large enough.

Contour plots of the eigenfunctions verify the salient feature of Hocking's asymptotic solution – a spanwise oscillation near the minor axis of about the right wavelength – but also indicate unexpectedly large flows away from the central region. Figures 5, 6 and 7 clearly show the presence of intense vortices in the axial (streamwise) velocity component along the critical layer at lateral stations far removed from the central minor axis. These vortices appear to signal the end of the eigenfunction laterally caused by the increasingly stabilizing conditions as the end is approached and presumably arise through the focusing of energy along the critical layer. Tatsumi & Yoshimura (1990) observe a similar feature in their eigenfunctions (see their figure 5*b*).

In some sense, these eigenfunctions resemble WKBJ solutions (see Drazin 1974) where the turning point is, relatively speaking, a 'locally neutral' region indicated by the end of the vortices. Inwards towards the 'unstable' central region, the eigenfunctions grow and oscillate, whereas outwards towards the 'locally stable' end regions, they decay exponentially. The intensity of these vortices relative to the central core is, however, quite an unexpected singular feature. Judging by the ultimate success of Hocking's asymptotic result, or indeed its higher-order version (4.1), the effect of

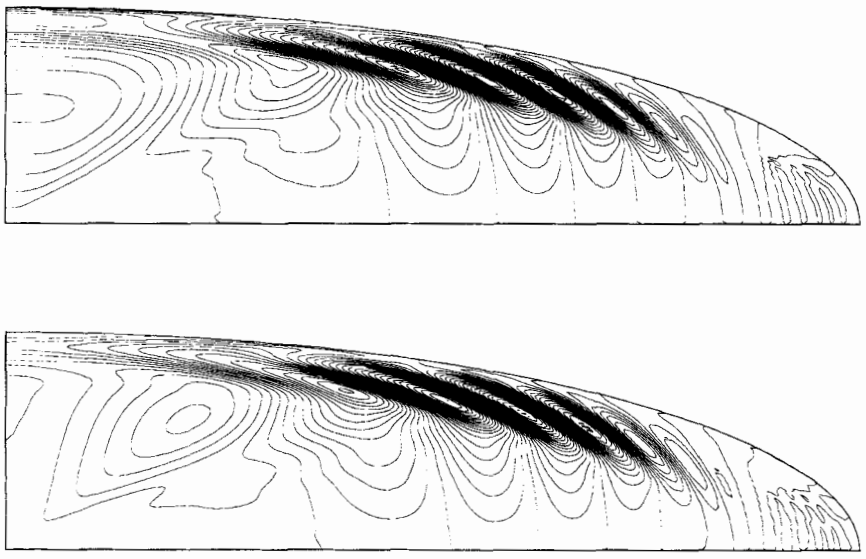

FIGURE 6. Contour plots of the axial velocity component (upper plot is Re(w) and lower Im(w)) just above criticality ($Re_{ppf} = 14\,600$, $\alpha_{ppf} = 0.91$, $c_r = 0.212888$) for a pipe of aspect ratio $A = 20$. The plot has been scaled down laterally by a factor of 5 and only the first quadrant is shown (there is symmetry with respect to the minor vertical axis and antisymmetry about the major horizontal axis). The truncation used is $N = 60$ and $M = 50$. The phase of the eigenfunctions has been chosen so that $\mathrm{Im}(w(x = 0, y = 0.5)) = 0$ and then normalized (max Re(w) = 1, max Im(w) = 0.966). The contour interval in both plots is 0.05.

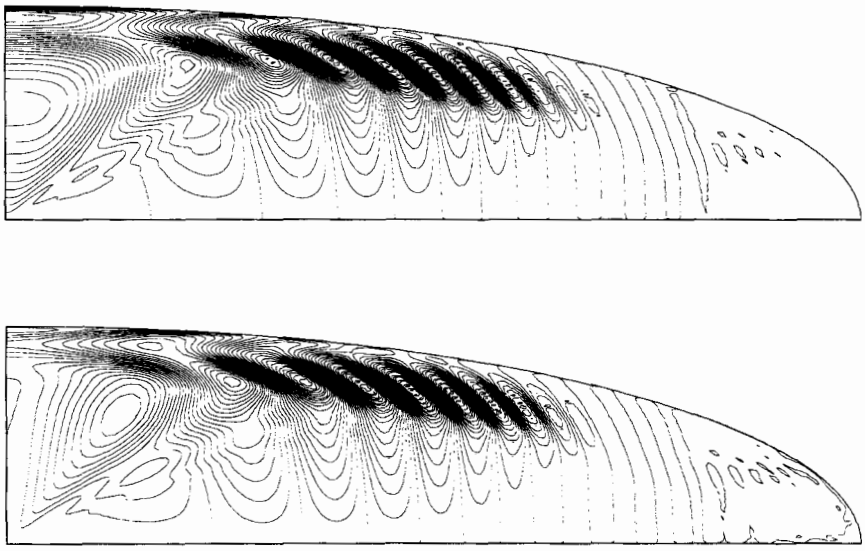

FIGURE 7. Contour plots of the axial velocity component (upper plot is Re(w) and lower Im(w)) just supercritical ($Re_{ppf} = 8\,100$, $\alpha_{ppf} = 0.9775$, $c_r = 0.244040$) for a pipe of aspect ratio $A = 50$. The plot has been scaled down laterally by a factor of 12.5(!) and only the first quadrant is shown (There is symmetry with respect to the minor vertical axis and antisymmetry about the major horizontal axis.). The truncation used is $N = 55$ and $M = 60$. The phase of the eigenfunctions has been chosen so that $\mathrm{Im}(w(x = 0, y = 0.5)) = 0$ and then normalized (max Re(w) = 0.987, max Im(w) = 1). The contour interval in both plots is 0.05. The eigenfunctions are clearly vanishingly small beyond the vortices in this extreme geometry.

these vortices on the damping rate must be at a higher order than that produced by the boundary curvature in the central region.

5. Discussion

In this paper, we have considered the linear stability of elliptic pipe flow at finite and large aspect ratios. A comprehensive survey at moderate aspect ratios ($A \leqslant 5$) indicated no special intermediary instability, emphasizing instead the robust stability of pipe flow. By numerical necessity, the search was then specialized to track the spanwise-modulated analogue of the unstable PPF Orr–Sommerfeld mode. Formally, the neutral curve so obtained only guarantees instability rather than making any statement about stability. Without a full survey establishing the stability of all eigenvalues 'below' this curve, we cannot be sure to have captured the actual neutral curve. It perhaps goes without saying that such a survey is well beyond reach numerically given that we have only just managed to resolve the simplest mode using an efficient inverse iterative approach. However, given the initial survey at moderate aspect ratios, we are fairly confident that the neutral curve shown in figure 3 is the real neutral curve. This conclusion is further supported by the stability picture of rectangular duct flow painted by Tatsumi & Yoshimura (1990). Here, even though the basic flow differs more substantially from PPF than elliptic pipe flow owing to the corners, the neutral curve is still found to be determined by the spanwise-modulated PPF mode.

The neutral curve depicted in figure 3 suggests a critical aspect ratio A_{crit} for linear instability of just over 10 (an exponential Shanks extrapolation gives a figure of ≈ 10.4). Intuitively, this seems reasonable as then the spanwise length scale is an order of magnitude larger than the streamwise length scale and one would imagine that the flow would be more PPF than HPF in character. However, as Hocking's work suggested, the critical Reynolds number is surprisingly sensitive to the aspect ratio, still being about 8000 at $A = 50$. Despite the presence of unexpectedly intense vortical structures along the critical layer at the spanwise ends of the eigenfunctions, Hocking's asymptote appears to be ultimately approached. This vindicates his working assumption that only the boundary curvature at the centre is important to leading order *for the linear damping rates* in elliptic pipe flow.

Unfortunately, figure 3 leaves one issue unresolved: does the critical Reynolds number tend to infinity or a finite value as $A \to A_{crit}$ from above? Certainly, if anything, the former scenario is suggested by figure 3. However, the latter can be argued for as follows. The growth rate of the one unstable Orr–Sommerfeld mode of PPF increases from 0 at $Re_{ppf} = 5772$, quickly reaches a maximum at just below $Re_{ppf} = 50\,000$ and then gradually decreases to 0 as $Re_{ppf} \to \infty$. Intuitively, one could imagine that introducing stabilizing sidewalls, or more to the point convex spanwise boundary curvature, would lower this curve, producing also an upper critical Reynolds number *just for this mode* (the situation for other three-dimensional modes is uncertain). In other words, decreasing A from infinity would close the neutral stability curve in the (α,Re)-plane for the spanwise modulated PPF mode. As A approaches A_{crit} (being close enough so that there are no unstable three-dimensional PPF modes), then the full neutral curve for elliptic pipe flow would be a shrinking *closed region* in the (α,Re)-plane enclosing a finite critical Reynolds number. However, the steepness of the neutral curve and the potential magnitude of any finite limiting Reynolds number indicated by figure 3 suggest that this issue is only of academic interest.

We are grateful to Professor A. M. Soward for a helpful discussion concerning the interpretation of figures 5, 6 and 7.

Appendix. Symmetries in polar coordinates

The symmetry results presented here are to greater or lesser extent already known and in use (e.g. Patera & Orszag 1981). However, that their origin should be so simple and generic appears to have escaped notice. (A notable exception to this is an appendix by Hollerbach & Ierley (1991) in which radial parities are discussed for axisymmetric variables in spherical polars.) As a result, it seemed desirable to collect together here these results for both cylindrical and spherical polar coordinates.

Cylindrical polar coordinates

Cylindrical polar coordinates are degenerate in the sense that both labels (s, ϕ, z) and $(-s, \phi \pm \pi, z)$ refer to the same point in physical space. Hence all physical quantities, whether a scalar p or a vector $\boldsymbol{u}$, must be invariant under the transformation

$$\mathscr{F} : (s, \phi) \rightarrow (-s, \phi \pm \pi). \tag{A 1}$$

If the azimuthal dependence is simply $e^{im\phi}$ as is typically the case in spectral expansions, this translates into the symmetry conditions in s:

$$\left.\begin{aligned} p(-s, z) &= (-1)^m p(s, z), \\ \boldsymbol{u}(-s, \phi \pm \pi) &= (-1)^m \boldsymbol{u}(s, \phi). \end{aligned}\right\} \tag{A 2}$$

Once the images of the base vectors under the $\mathscr{F}$ are taken into account,

$$\hat{\boldsymbol{s}}(-s, \phi \pm \pi) = -\hat{\boldsymbol{s}}(s, \phi), \quad \hat{\boldsymbol{\phi}}(-s, \phi \pm \pi) = -\hat{\boldsymbol{\phi}}(s, \phi),$$

we obtain parity conditions on the individual velocity components

$$u_s(-s, z) = -(-1)^m u_s(s, z), \tag{A 3}$$

$$u_\phi(-s, z) = -(-1)^m u_\phi(s, z), \tag{A 4}$$

$$u_z(-s, z) = +(-1)^m u_z(s, z). \tag{A 5}$$

It is worth re-emphasizing that these symmetries are inherent to the coordinate representation rather than indicative of any feature of the equations being solved. It should also be stressed that these ideas are only useful if the axis $s = 0$ is included in the domain of interest, otherwise they are trivially observed. This is best illustrated by the simple solution $\Phi = (As + Bs^{-2})\cos\phi$ to Laplace's equation which should be more accurately written as $\Phi = (As + Bs^{-1}|s|^{-1})\cos\phi$. Obviously, the presence of $|s|$ would only lead to discontinuities in the physical variables and hence be disallowed if the axis is part of the domain.

Spherical polar coordinates

The arguments presented above may be repeated for spherical polar coordinates, where the labels (r, θ, ϕ), $(-r, \theta \pm \pi, \phi)$, $(-r, \pm\pi - \theta, \phi \pm \pi)$ and $(r, -\theta, \phi \pm \pi)$ are all equivalent. These degeneracies are encapsulated by the invariance of physical quantities under the two transformations:

$$\mathscr{F}_1 : (r, \theta, \phi) \rightarrow (r, -\theta, \phi \pm \pi) \tag{A 6}$$

where

$$\hat{\boldsymbol{r}}(-\theta, \phi \pm \pi) = +\hat{\boldsymbol{r}}(\theta, \phi), \quad \hat{\boldsymbol{\theta}}(-\theta, \phi \pm \pi) = -\hat{\boldsymbol{\theta}}(\theta, \phi), \quad \hat{\boldsymbol{\phi}}(-\theta, \phi \pm \pi) = -\hat{\boldsymbol{\phi}}(\theta, \phi),$$

and

$$\mathscr{F}_2 : (r, \theta, \phi) \rightarrow (-r, \theta \pm \pi, \phi) \tag{A 7}$$

where

$$\hat{\boldsymbol{r}}(\theta \pm \pi, \phi) = -\hat{\boldsymbol{r}}(\theta, \phi), \quad \hat{\boldsymbol{\theta}}(\theta \pm \pi, \phi) = -\hat{\boldsymbol{\theta}}(\theta, \phi), \quad \hat{\boldsymbol{\phi}}(\theta \pm \pi, \phi) = +\hat{\boldsymbol{\phi}}(\theta, \phi).$$

As before, if we assume that the azimuthal dependence is merely $\mathrm{e}^{\mathrm{i}m\phi}$, invariance under $\mathscr{F}_1$ means that

$$\left.\begin{aligned} p(r, -\theta) &= +(-1)^m p(r, \theta), \\ u_r(r, -\theta) &= +(-1)^m u_r(r, \theta), \\ u_\theta(r, -\theta) &= -(-1)^m u_\theta(r, \theta), \\ u_\phi(r, -\theta) &= -(-1)^m u_\phi(r, \theta), \end{aligned}\right\} \tag{A 8}$$

whereas invariance under $\mathscr{F}_2$ leads to

$$\left.\begin{aligned} p(-r, \theta \pm \pi) &= +p(r, \theta), \\ u_r(-r, \theta \pm \pi) &= -u_r(r, \theta), \\ u_\theta(-r, \theta \pm \pi) &= -u_\theta(r, \theta), \\ u_\phi(-r, \theta \pm \pi) &= +u_\phi(r, \theta). \end{aligned}\right\} \tag{A 9}$$

As an example of how these relations can be exploited, we consider a specific but common situation in which the velocity field $\boldsymbol{u}$ in a spherically symmetric system is decomposed into toroidal and poloidal components:

$$\boldsymbol{u} = \nabla \times (e\hat{\boldsymbol{r}}) + \nabla \times \nabla \times (f\hat{\boldsymbol{r}}). \tag{A 10}$$

It is fairly standard to expand e and f using spherical harmonics as follows:

$$e = \sum_l e_l(r) P_l^m(\cos\theta)\mathrm{e}^{\mathrm{i}m\theta}, \quad f = \sum_n f_n(r) P_n^m(\cos\theta)\mathrm{e}^{\mathrm{i}m\theta},$$

(where P_l^m is the associated Legendre polynomial of degree l and order m) which means that

$$\left.\begin{aligned} u_r &= \sum_n \frac{n(n+1)}{r^2} f_n(r) P_n^m(\cos\theta)\mathrm{e}^{\mathrm{i}m\phi}, \\ u_\theta &= \sum_l \frac{\mathrm{i}m}{r} e_l(r) \frac{P_l^m(\cos\theta)}{\sin\theta}\mathrm{e}^{\mathrm{i}m\phi} + \sum_n \frac{1}{r}\frac{\mathrm{d}f_n(r)}{\mathrm{d}r}\frac{\mathrm{d}P_n^m(\cos\theta)}{\mathrm{d}\theta}\mathrm{e}^{\mathrm{i}m\phi}, \\ u_\phi &= -\sum_l \frac{1}{r} e_l(r) \frac{\mathrm{d}P_l^m(\cos\theta)}{\mathrm{d}\theta}\mathrm{e}^{\mathrm{i}m\phi} + \sum_n \frac{\mathrm{i}m}{r}\frac{\mathrm{d}f_n(r)}{\mathrm{d}r}\frac{P_n^m(\cos\theta)}{\sin\theta}\mathrm{e}^{\mathrm{i}m\phi}. \end{aligned}\right\} \tag{A 11}$$

These automatically satisfy the conditions (A 8) because

$$P_l^m \rightarrow (-1)^m P_l^m \quad \text{under} \quad \theta \rightarrow -\theta. \tag{A 12}$$

The even or oddness of $l - m$ and $n - m$ determines the particular symmetries of the velocity field about the equator $\theta = \pi/2$: for instance if u_ϕ is symmetric about the equator, $l - m$ must be odd and $n - m$ even as

$$P_l^m \rightarrow (-1)^{l-m} P_l^m \quad \text{under} \quad \theta \rightarrow \pi - \theta. \tag{A 13}$$

The conditions (A 9) then dictate the radial symmetries through

$$P_l^m \to (-1)^l P_l^m \quad \text{under} \quad \theta \to \theta \pm \pi, \tag{A 14}$$

as follows:

$$e_l(-r) = -(-1)^l e_l(r), \quad f_n(-r) = -(-)^n f_n(r). \tag{A 15}$$

REFERENCES

BATCHELOR, G. K. & GILL, A. E. 1962 Analysis of the stability of axisymmetric jets. *J. Fluid Mech.* **14**, 529–551.

COWLEY, S. J. & SMITH, F. T. 1985 On the stability of Poiseuille–Couette flow: a bifurcation from infinity. *J. Fluid Mech.* **156**, 83–100.

DAVEY, A. 1978 On the stability of flow in an elliptic pipe which is nearly circular. *J. Fluid Mech.* **87**, 233–241.

DAVEY, A. & NGUYEN, H. P. F. 1971 Finite-amplitude stability of pipe flow. *J. Fluid Mech.* **45**, 701–720.

DAVEY, A. & SALWEN, H. 1994 On the stability of flow in an elliptic pipe which is nearly circular. *J. Fluid Mech.* **281**, 357–369.

DRAZIN, P. G. 1974 On a model of instability of a slowly-varying flow. *Q. J. Mech. Appl. Maths* **27**, 69–86.

GILL, A. E. 1973 The least-damped disturbance to Poiseuille flow in a circular pipe. *J. Fluid Mech.* **61**, 97–107.

HAINS, F. D. 1967 Stability of plane Couette–Poiseuille flow. *Phys. Fluids* **10**, 2079–2080.

HOCKING, L. M. 1977 The stability of flow in an elliptic pipe with large aspect ratio. *Q. J. Mech. Appl. Maths* **30**, 343–353.

HOCKING, L. M. 1978 Nonlinear instability of flow in a rectangular pipe with large aspect ratio. *J. Appl. Maths. Phys.* **29**, 100–111.

HOLLERBACH, R. & IERLEY, G. R. 1991 A modal α^2-dynamo in the limit of asymptotically small viscosity. *Geophys. Astrophys. Fluid Dyn.* **56**, 133–158.

KERSWELL, R. R. 1994 Tidal excitation of hydromagnetic waves and their damping in the Earth. *J. Fluid Mech.* **274**, 219–241.

MACKRODT, P.-A. 1976 Stability of Hagen–Poiseuille flow with superimposed rigid rotation. *J. Fluid Mech.* **73**, 153–164.

ORSZAG, S. A. 1971 Accurate solution of the Orr–Sommerfeld stability equation. *J. Fluid Mech.* **50**, 689–703.

O'SULLIVAN, P. L. & BREUER, K. S. 1994 Transient growth in circular pipe flow. I. Linear disturbances. *Phys. Fluids* **6**, 3643–3651.

PATERA, A. T. & ORSZAG, S. A. 1981 Finite amplitude stability of axisymmetric pipe flow. *J. Fluid Mech.* **112**, 467–474.

POTTER, M. C. 1966 Stability of plane Couette–Poiseuille flow. *J. Fluid Mech.* **24**, 609–619.

REYNOLDS, W. C. & POTTER, M. C. 1967 Finite-amplitude instability of parallel shear flow. *J. Fluid Mech.* **27**, 465–492.

SCHMID, P. J. & HENNINGSON, D. S. 1994 Optimal energy density growth in Hagen–Poiseuille flow. *J. Fluid Mech.* **277**, 197–225.

SMITH, F. T. 1979 Instability of flow through pipes of general cross-section. Parts I and II. *Mathematika* **26**, 187–210, 211–223.

TATSUMI, T. & YOSHIMURA, T. 1990 Stability of laminar flow in a rectangular duct. *J. Fluid Mech.* **212**, 437–449.